

AD-A097 982

SRI INTERNATIONAL MENLO PARK CA
PARTICLE IMPACT DAMAGE IN CERAMICS. (U)
MAR 81 D A SHOCKEY, K C DAO, D C ERLICH

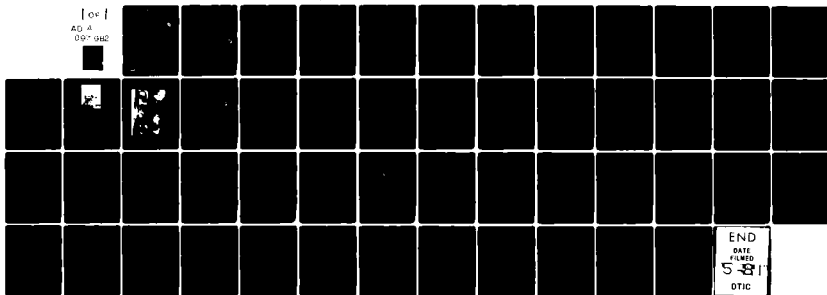
F/6 11/2

UNCLASSIFIED

N00014-76-C-0657

NL

[00]
AD A
007 980



END
DATE
FILMED
5-81
DTIC

LEVEL



**PARTICLE IMPACT DAMAGE
IN CERAMICS**

AD A 197982

Annual Report--Part IV

March 1981

NOTICED
APR 20 1981

By: D. A. Shockey

Contributors: R. L. Burback
D. R. Curran
K. C. Dao
D. C. Erlich
L. Seaman

Prepared for:

Office of Naval Research
800 N. Quincy Street
Arlington, VA 22217

Attention: Dr. R. C. Pohanka

Contract No. N00014-76-C-0657
Contract Authority No. NR 023-563/2-02-79(471)

SRI Project PYU 4928

Approved for public release: distribution unlimited.

Reproduction in whole or in part is permitted
for any purpose of the United States Government.

SRI International
333 Ravenswood Avenue
Menlo Park, California 94025
(415) 326-6200
Cable: SRI INTL MPK
TWX: 910-373-1246

copy



81 4 20 029

UNCLASSIFIED

SECURITY CLASSIFICATION OF THIS PAGE (When Data Entered)

REPORT DOCUMENTATION PAGE		READ INSTRUCTIONS BEFORE COMPLETING FORM
1. REPORT NUMBER	2. GOVT ACCESSION NO	3. RECIPIENT'S CATALOG NUMBER
	AD-A097982	(9)
4. TITLE (and Subtitle)	5. NAME OF REPORT & PERIOD COVERED	
PARTICLE IMPACT DAMAGE IN CERAMICS.	Annual Report - Part IV 8 Feb 79-7 Feb 80	
	6. PERFORMING ORG. REPORT NUMBER	
7. AUTHOR(s)	8. CONTRACT OR GRANT NUMBER(s)	
D. A. Shockey Contributors: R. L. Burback D. R. Curran K. C. Dao D. C. Erlich L. Seaman	N00014-76-C-0657	
9. PERFORMING ORGANIZATION NAME AND ADDRESS	10. PROGRAM ELEMENT PROJECT, TASK AREA & WORK UNIT NUMBERS	
SRI International 333 Ravenswood Avenue Menlo Park, CA 94025	NR 032-563/2-02-79(471)	
11. CONTROLLING OFFICE NAME AND ADDRESS	12. REPORT DATE	13. NUMBER OF PAGES
Office of Naval Research 800 N. Quincy Avenue Arlington, VA 22217	March 1981	56
14. MONITORING AGENCY NAME & ADDRESS (if different from Controlling Office)	15. SECURITY CLASS (of this report)	
Dr. R. C. Pohanka Office of Naval Research 800 N. Quincy Street Arlington, VA 22217	UNCLASSIFIED	
16. DISTRIBUTION STATEMENT (of this Report)	15a. DECLASSIFICATION DOWNGRADING SCHEDULE	
Approved for public release; distribution unlimited.		
17. DISTRIBUTION STATEMENT (of the abstract entered in Block 20, if different from Report)		
18. SUPPLEMENTARY NOTES		
19. KEY WORDS (Continue on reverse side if necessary and identify by block number)		
Si ₃ N ₄ , ZnS, Si ₃ N ₄ -20%ZrO ₂ , particle impact, fracture damage, effect of temperature, dynamic hardness, oxidation toughening, transformation toughening, predictive capability, stress field history computation, fracture model, crack nucleation, crack growth.		
20. ABSTRACT (Continue on reverse side if necessary and identify by block number)		
Impacts of tungsten carbide spheres on Si ₃ N ₄ produced elastic fracture behavior (ring and cone cracks) at room temperature, but elastic-plastic fracture behavior (plastic impressions and radial cracks) at 1400°C. In contrast, no change in fracture pattern at the two temperatures was produced by impact with steel spheres. These results may be explained by the relative abilities of the impacting spheres to cause plastic flow at the impact site and hence to alter the stress distribution in the Si ₃ N ₄ specimens.		

DTIC
SELECTED
APR 20 1981
C

DD FORM 1473

1 JAN 73

EDITION OF 1 NOV 65 IS OBSOLETE

UNCLASSIFIED

SECURITY CLASSIFICATION OF THIS PAGE (When Data Entered)

(Abstract concluded)

The type and extent of damage produced by hard particle impact at 1400°C appears to be more deleterious to structural integrity than that produced at 20°C under equivalent particle impact loading conditions.

When impacted by 1.2-mm-diameter tungsten carbide spheres at velocities to 200 m/s, oxidized Si₃N₄-20 vol% ZrO₂ exhibited decidedly less fracture damage than unoxidized material. The impact velocity necessary to initiate ring and radial cracks was significantly higher for oxidized materials, and the rate at which fracture damage, once nucleated, developed was substantially lower. This enhanced dynamic performance is consistent with the enhanced quasi-static properties reported by Lange and may involve oxidation-induced compressive surface stresses, oxidation-induced softening, or both.

Progress is reported in the development of a predictive capability for fracture damage produced by particle impact. Efforts were directed toward computing stress field histories in the vicinity of an impact site, and constructing mathematical expressions describing the development of cracks.

A finite difference code TROTT was provided with slide lines to simulate particle impact of a ZnS plate, accounting for plastic flow but not fracture. Good quantitative agreement was obtained with experimental measurements of rebound velocity and crater dimensions at low impact velocities (low fracture damage). A fracture model consisting of functional forms of expressions for crack nucleation and growth, and a methodology for crack-induced stress relaxation, is described.

Accession For	<input checked="" type="checkbox"/>
NTIS GRA&I	<input type="checkbox"/>
DTIC TAB	<input type="checkbox"/>
Unannounced	<input type="checkbox"/>
Justification	
By	
Distribution	
Availability	
Dist	

A

CONTENTS

1	INTRODUCTION AND OBJECTIVES	1
1.1	Introduction	1
1.2	Objectives	1
2	PARTICLE IMPACT DAMAGE IN Si_3N_4 AT 1400°C	3
2.1	Background	3
2.2	Experimental	3
2.3	Results	5
2.4	Discussion	6
2.5	Conclusions and Recommendations	12
3	IMPROVED IMPACT FRACTURE RESISTANCE IN OXIDATION-TOUGHENED Si_3N_4 + 20vol% ZrO_2	13
3.1	Background	13
3.2	Materials, Experiments, and Results	13
3.3	Discussion	16
4	PROGRESS IN DEVELOPING A PREDICTIVE CAPABILITY FOR HARD PARTICLE IMPACT DAMAGE IN CERAMICS	21
4.1	Approach	21
4.2	Calculation of the Stress Field History in a Plate Impacted by a Sphere	23
4.2.1	Background	23
4.2.2	Computational Procedure	24
4.2.3	Results	26
4.3	Construction of a Computational Fracture Model	34
4.3.1	Phenomenology of Particle Damage in ZnS	36
4.3.2	Rudiments of the Fracture Model	37
4.4	Future Work	42
4.5	Summary	44
	REFERENCES	47

ILLUSTRATIONS

1. High Temperature Particle Impact Facility	4
2. Plastic Impression Diameter Versus Impact Velocity for HP Si_3N_4 at Room Temperature and 1400°C (2.4-mm-dia. WC spheres)	7
3. Surface Damage in Si_3N_4 Produced by 50 m/s Impact of Tungsten Carbide Spheres at Two Temperatures	8
4. Side Views of Specimen Fractured by an Impacting Tungsten Carbide Sphere	9
5. Surface Damage in Si_3N_4 Produced at Two Temperatures by Impact of a 2.4-mm-diameter Steel Sphere	10
6. Plastic Impression Diameter Versus Impact Velocity for Oxidized and Unoxidized Si_3N_4 -20 vol% ZrO_2	15
7. Surface Damage Produced by Particle Impact at 145 m/s	17
8. Growth of Damage Zone with Impact Velocity for Oxidized and Unoxidized Si_3N_4 -20 vol% ZrO_2	18
9. Computational Grids Used in Simulating a Sphere Impacting a Plate	28
10. Stress-Strain Curve for ZnS Indented with an 800- μm - dia. WC Sphere	29
11. Variation of Tangential Tensile Stress With Time at 1, 1.5, 2 and 3 Crater Radii (r) From Impact Site	32
12. Variation of Peak Tangential Tensile Stress with Distance from Impact Site for Three Impact Velocities	33
13. Residual Stress Field in ZnS after Impact with an 800- μm -dia. WC Sphere at Three Velocities	35

TABLES

I Material Properties Used in Particle Impact Simulation	27
II Comparison of Computed and Observed Results of Particle Impact Experiments	31

ACKNOWLEDGMENTS

Thanks are due to D. J. Rowcliffe and D. B. Marshall for reviewing parts of the manuscript. The authors also thank Dr. F. F. Lange of Rockwell International for providing the specimens discussed in Section 3.

1 INTRODUCTION AND OBJECTIVES

1.1 Introduction

Materials having acceptable radiation transmission properties for use as infrared windows and radomes on aircraft generally have poor resistance to fracture in particle impact situations. The microfractures that form and grow under bombardment by rain, dust, and ice particles scatter incident radiation and result in continuous degradation of the optical properties with flight time. Longer exposures or more severe impact environments can result in interaction of microfractures with each other and with the radome surfaces, causing mass loss (erosion) and gross mechanical failure. Erosion and gross failure behavior at high temperature must also be considered in designing ceramic components of turbine engines. The Navy wishes to ascertain high temperature failure mechanisms, to establish more impact-resistant microstructural forms of ceramic materials and to develop a capability for predicting the fracture behavior. In support of these needs, SRI International is performing research to understand failure behavior of Si_3N_4 at turbine engine operating temperatures, to examine failure behavior of microstructurally toughened Si_3N_4 and to establish expressions and material properties governing fracture development in ceramic window, radome, and engine materials under hard particle impact.

1.2 Objectives

This annual technical report documents the results and progress attained during the fourth year of a research program aimed at solving specific problems of impact damage of ceramics.

The three specific objectives in this fourth year were to:

- (1) Determine the erosion behavior of Si_3N_4 at 1400°C (gas turbine operating temperature) and note differences and similarities with room temperature behavior.

- (2) Ascertain the erosion performance of a microstructurally toughened $\text{Si}_3\text{N}_4\text{-ZrO}_2$ ceramic and compare the results with untoughened material.
- (3) Develop a predictive capability for calculating fracture damage in ceramics caused by particle impact.

Completed accounts of the work on objectives 1 and 2 are presented here as Sections 2 and 3, and have been accepted for publication in the Bulletin of the American Ceramic Society and the Journal of Materials Science, respectively. The progress and status of the effort on objective 3 are reported in Section 4.

2 PARTICLE IMPACT DAMAGE IN SILICON NITRIDE AT 1400°C

2.1 Background

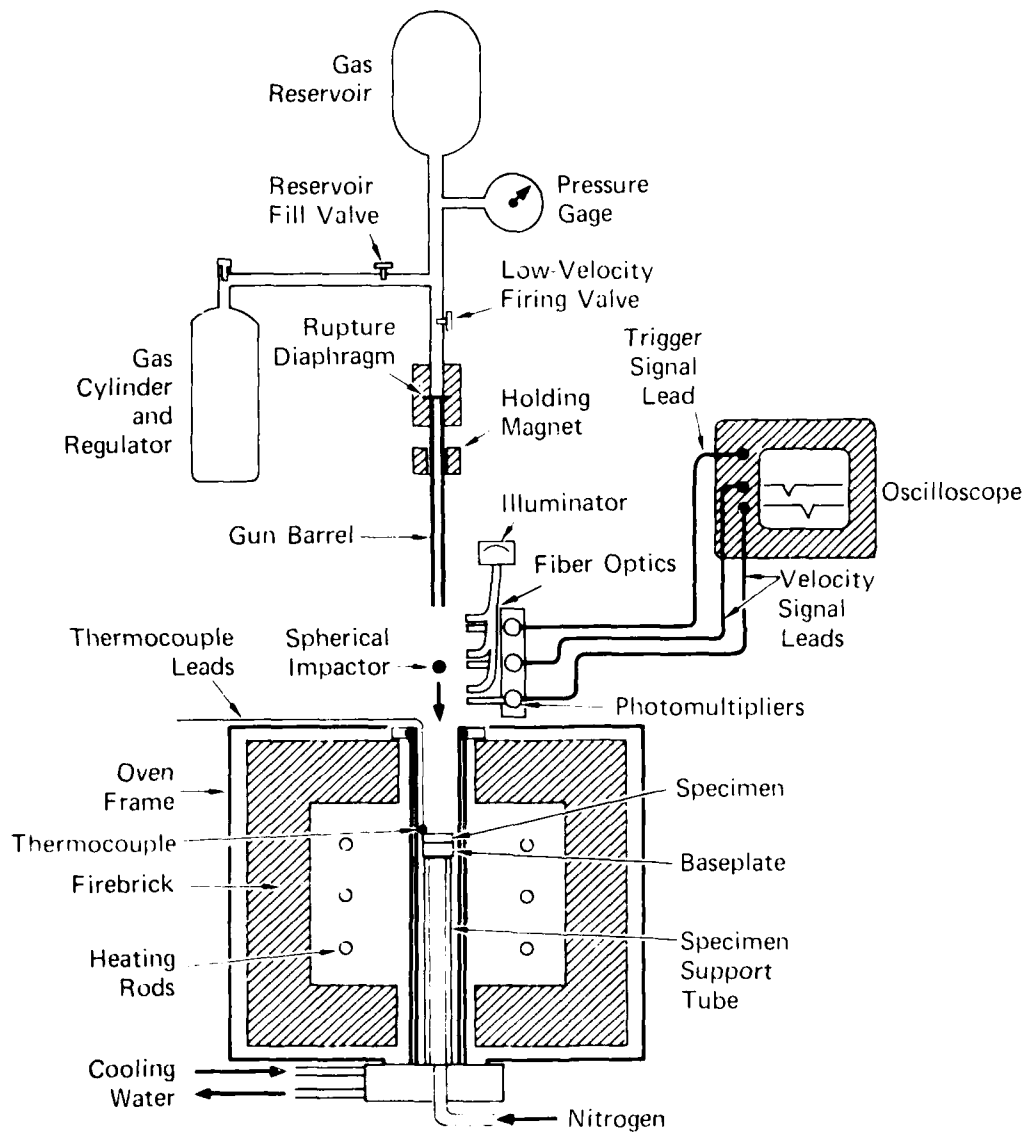
The properties of silicon nitride--high strength at elevated temperatures, low density, low coefficient of thermal expansion, and high oxidation resistance--make it an attractive low-cost alternative to superalloys for stators, rotors and other high-temperature engine components. A major concern, however, with using silicon nitride components in flying turbines is the sensitivity of their load-bearing capacity to flaws and cracks. Aircraft turbine engines ingest solid particles during flight, and the resulting impacts can produce cracks that could reduce the strength below that necessary to sustain design loads, thereby causing catastrophic failure.

Recent research efforts (Reference 1, for example) have established the failure phenomenology and the strength degradation effects² of impact-induced cracks in Si_3N_4 at room temperatures. However, similar information is lacking at the elevated temperature representative of gas turbine service conditions. This section describes initial results of impact experiments on Si_3N_4 at 1400°C and compares the damage observations with those from room temperature experiments.

2.2 Experimental

Octagonal specimens roughly 25 mm in diameter were cut from a 6.35-mm-thick plate of fully dense NC132 hot pressed silicon nitride (HP Si_3N_4) purchased from the Norton Company, Worcester, Mass. The microstructure consisted of β - Si_3N_4 grains, most of which were equiaxed and less than 1 μm in size, although some were up to 4 μm long with aspect ratios up to 10. No significant grain boundary or inclusion phases were observed, but traces of tungsten carbide and tungsten disilicide were detected by x-ray diffraction.

The impact side of the specimens was polished and the specimens were placed into a central vertical refractory tube of a furnace onto a 12-mm-thick silicon nitride slab supported by an inner tube. The



MA-4928-102

FIGURE 1 HIGH TEMPERATURE PARTICLE IMPACT FACILITY

particle impact facility is shown in Figure 1. To reduce possible effects of stress wave reflections from the rear specimen surface, the mating surfaces of specimen and slab were also ground flat and polished. The temperature of the specimens was increased to $1380 \pm 20^\circ\text{C}$ in about 3 hours and maintained at this level for the particle impact experiments. A platinum-rhenium thermocouple monitored the temperature at the specimen location. While they were at elevated temperature, the specimens were bathed in a stream of nitrogen gas to reduce surface oxidation.

Single spheres of tungsten carbide or steel 2.4 mm in diameter were accelerated in a small gun barrel by the sudden release of compressed air. A thin disk located between the gas reservoir and the gun barrel sustained the compressed air until a pressure was reached that caused the disk to rupture. Rupture pressure, and hence particle velocity, was varied by using disks of different materials and thicknesses. Velocities below 85 m/s were achieved by omitting the rupture disk, pressurizing the compressed air reservoir to a desired low pressure, and opening the valve by hand. Impact velocities were measured by the photomultiplier arrangement. Light reflected by the particle into a photomultiplier at three fixed stations indicated particle position at three times during its flight to the target.

2.3 Results

Room temperature experiments were carried out¹ at velocities ranging from 7 to 230 m/s. No damage was produced by impacts with 2.4-mm-diameter tungsten carbide spheres at velocities less than 15 m/s. A partial ring crack appeared at 15 m/s. Velocities between 15 and 30 m/s produced ring cracks of increasing number and size, and velocities between 30 and 90 m/s produced ring cracks, cone cracks, and a plastic impression. Above 90 m/s, radial cracking as well as fragmentation of the tungsten carbide sphere occurred.

Impact experiments at 1400°C were performed at velocities of 38, 51, 85, 121, 156, 173, and 197 m/s with tungsten carbide spheres. Radial

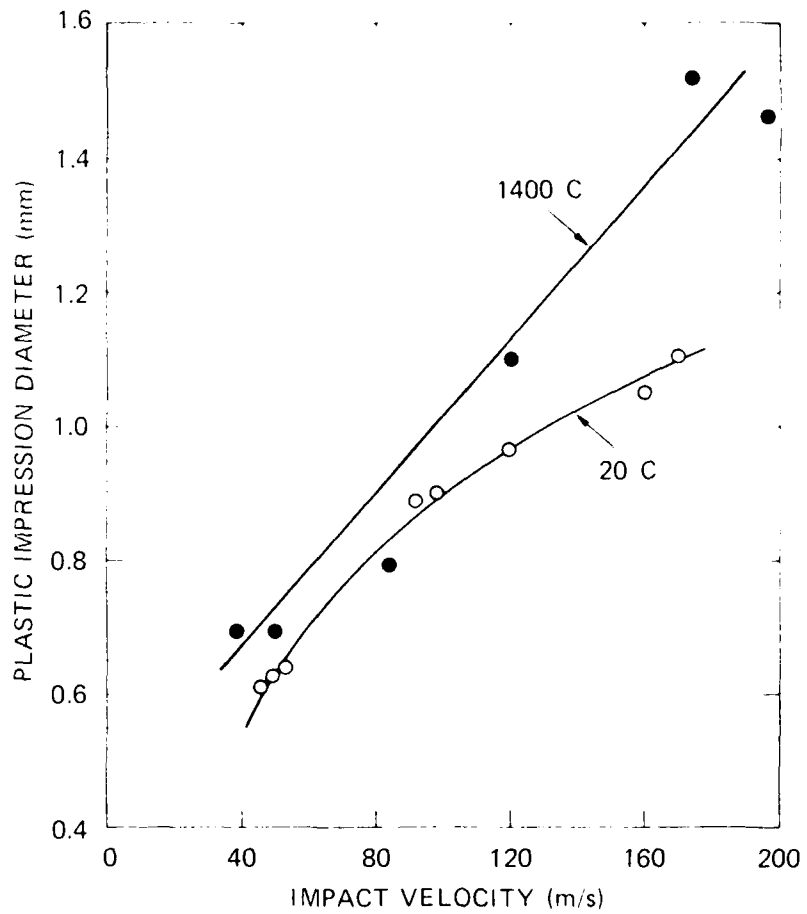
cracks and a well-defined plastic impression were produced in each experiment. As shown in Figure 2, the size of the impression and intensity of the radial cracks increased with increasing velocity. At velocities greater than 150 m/s, the radial cracks extended to the sides and rear surfaces of the specimens, often fragmenting them. Figure 3 compares the damage at 20°C and 1400°C produced by tungsten carbide spheres impacting at about 50 m/s. The type of damage at 1400°C (radial cracks) is more deleterious than the ring-cone cracking that occurs at 20°C because radial cracks tend to be longer and deeper. Moreover, the damaged surface area is substantially larger at 1400°C. The relative dynamic hardness at 1400°C, computed from the plastic impression diameters, Figure 2, using the Brinell equation, decreased monotonically from 0.8 at 50 m/s to about 0.6 at 170 m/s.

Cone cracks occurred along with radial and lateral cracks in Si_3N_4 at 1400°C, as evidenced by the cross section shown in Figure 4. This fracture surface, produced by extension of radial cracks, reveals the site of the cone-shaped fragment beneath the impact site, the lateral cracks that initiate internally near the boundary of the plastic zone, the profile of the radial cracks, and the microcracked zone directly beneath the plastic impression.

By contrast, the fracture damage produced by 2.4-mm-diameter steel spheres consisted of annuli of segmental ring cracks both at room temperature and at 1400°C, even at velocities of 230 m/s,¹ Figure 5. The threshold velocity for fracture at 20°C by steel spheres was about 40 m/s, or nearly three times as high as the threshold velocity for tungsten carbide spheres.

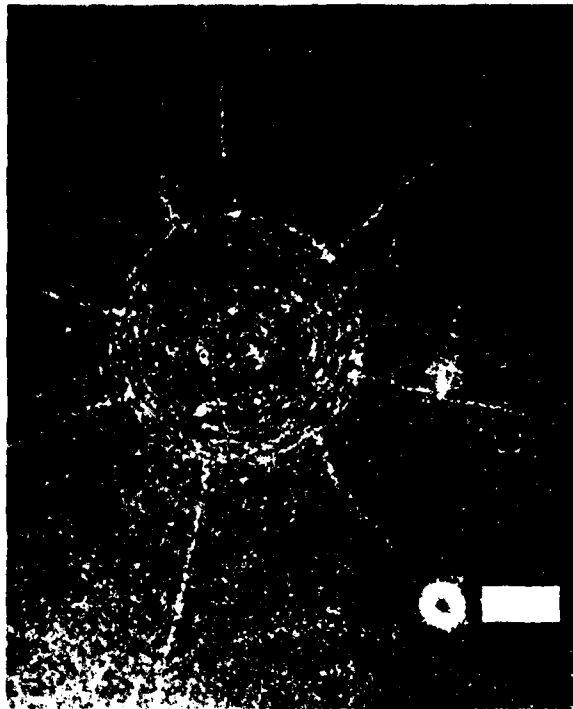
2.4 Discussion

These results show that the impact-induced fracture pattern in Si_3N_4 at 1400°C can be, but is not necessarily, different than that at 20°C. The behavior seems to depend on the hardness of the particle relative to the target, and can be explained by a difference in the near-crater stress distribution when elastic or plastic deformation occurs in the target.



MA-4928-104A

FIGURE 2 PLASTIC IMPRESSION DIAMETER VERSUS IMPACT VELOCITY FOR HP Si_3N_4 AT ROOM TEMPERATURE AND 1400 C (2.4-mm-dia. tungsten carbide spheres)



(a) 1400 C

200 μm

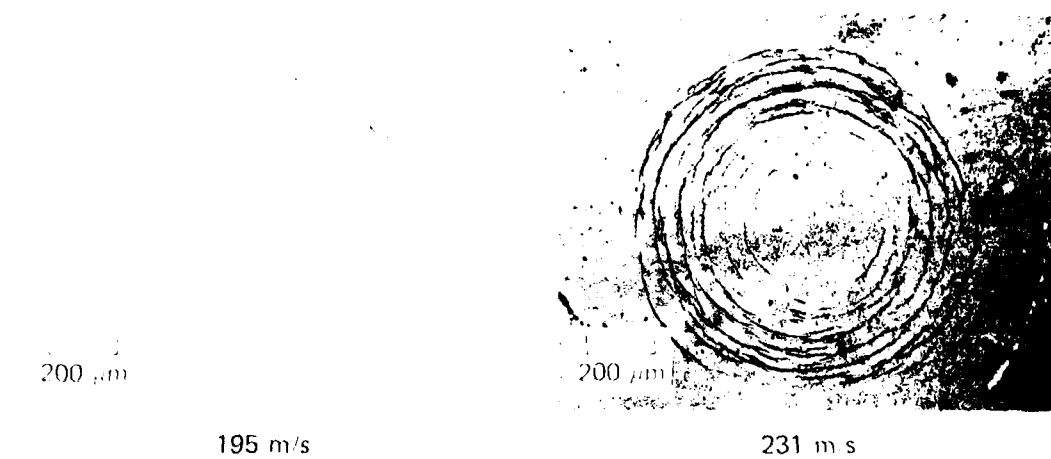
(b) 20 C

MP-4953-105

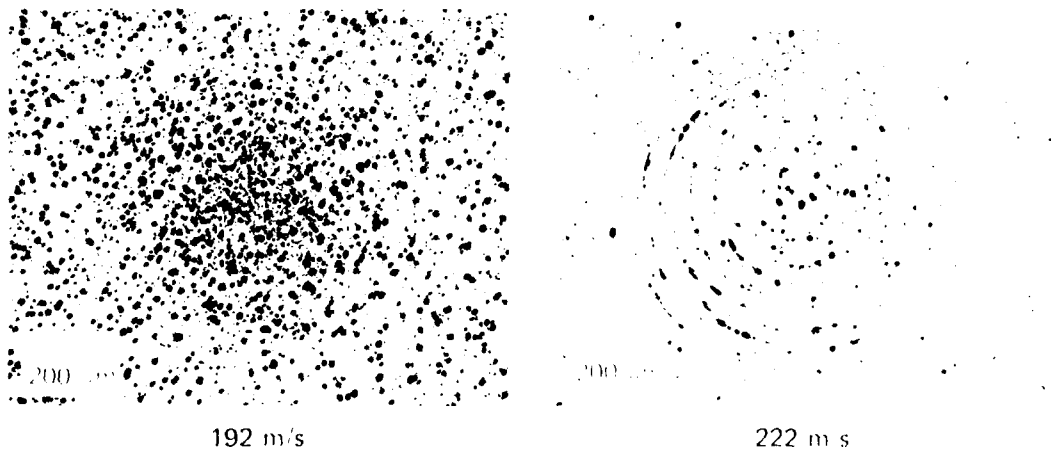
FIGURE 3 SURFACE DAMAGE IN S₁N₁ PRODUCED BY 50 m/s IMPACT OF TUNGSTEN CARBIDE SPHERES AT TWO TEMPERATURES



FIGURE 4 SIDE VIEWS OF SPECIMEN FRACTURED BY AN IMPACTING TUNGSTEN CARBIDE SPHERE



(a) ROOM TEMPERATURE



(b) 1370 C

NOTE: Surfaces in (b) lightly polished to remove oxide scale

FIGURE 5 SURFACE DAMAGE IN Si_3N_4 PRODUCED AT TWO TEMPERATURES BY IMPACT OF A 2.4 mm DIAMETER STEEL SPHERE

Evans, Lawn, and Wilshaw^{3,4} have explained the various cracking patterns observed in ceramics around indenters and impacting particles on the basis of differences in stress states caused by the absence or the occurrence of plastic flow. When the target deforms elastically, the maximum tensile stresses are directed radially, resulting in an annulus of segmented ring cracks just outside the circle of contact. Higher indentation pressures or impact velocities cause these shallow ring cracks, which grow initially nearly normal to the contact surface, to extend downward and away from the zone of compression under the contact site to form cone-shaped cracks with sides roughly 50° to the impact surface or 22° to the indentation surface.

When the material under the contact area deforms plastically, radial stresses relax and the stresses in the tangential direction become tensile, often resulting in the appearance of radial cracks extending outward from the periphery of the plastic impression in a spokelike array. Tensile stresses also arise in the specimen interior normal to the impacted surface, particularly during unloading, and may produce lateral cracks parallel to the specimen surface.

These considerations suggest that when the Si_3N_4 is at 1400°C , the relative hardnesses of Si_3N_4 and tungsten carbide may be reversed, allowing the tungsten carbide sphere to remain elastic and transmit loads to the Si_3N_4 target that exceed the high temperature yield strength of Si_3N_4 . In the case of steel spheres, if the hardness of Si_3N_4 at 1400°C remains greater than the room temperature hardness of the steel, then when impact occurs, the sphere would deform plastically, preventing loads in excess of the Si_3N_4 yield strength and resulting in elastic fracture.

These inferences are in accord with relative dynamic hardnesses estimated from static room temperature hardness values of 1600, 1570, and 820 kg/mm^2 measured for the silicon nitride plates, the tungsten carbide spheres, and the steel spheres, respectively. The impression diameter data in Figure 2 show that the hardness of Si_3N_4 at 1400°C is about 80% of the room temperature hardness, or about 1300 kg/mm^2 . Therefore, assuming similar rate effects for Si_3N_4 and WC, the WC

spheres should cause elastic fracture behavior in Si_3N_4 at room temperature, but elastic/plastic fracture behavior at 1400°C , as was observed. Furthermore, since the hardness of the steel spheres is far below the Si_3N_4 hardness even at 1400°C , steel spheres should produce only elastic fracture of the Si_3N_4 , also as observed. The slight differences in hardness of Si_3N_4 and WC (1600 versus 1570 kg/mm^2) will likely be enhanced in these experiments by the differences in geometry for the two materials. Geometries that constrain the plastically deformed zone more highly (such as the Si_3N_4 plate, which surrounds the plastic impression by a half space of bulk elastic material) will require higher loads for a given indentation than less constrained geometries⁵ (such as the small impacting sphere).

Studman and Field observed both radial and ring cracking in a quenched steel around indentations produced by tungsten carbide spheres and also explained the behavior in terms of a transition from elastic to elastic/plastic behavior.⁶

2.5 Conclusions and Recommendations

These results point to guidelines for predicting the type and extent of damage in Si_3N_4 turbine components to be expected from given debris particles. If indeed the relative hardnesses of particle and component govern the type of cracking in the component, a knowledge of the component hardness at the temperature of service and the hardness of the anticipated debris particles would indicate the fracture geometry and allow the propensity for strength degradation and erosion to be assessed. Cracks that tend to penetrate the component (radials, medians and cones) tend to degrade its strength, whereas cracks that tend to turn back to the surface (laterals and cones) tend to promote mass loss and erosion. A more quantitative predictive capability must await additional experiments that show the extent of damage and the resulting strength degradation and erosion behavior as a function of relative target and particle hardnesses, particle velocity, size, shape, and the number of impacts.

3 IMPROVED IMPACT FRACTURE RESISTANCE IN OXIDATION-TOUGHENED Si_3N_4 -20 VOL% ZrO_2

3.1 Background

An oxidation technique to induce compressive stresses in the near-surface regions of Si_3N_4 - ZrO_2 specimens has been reported by Lange.⁷ The material is made by thoroughly mixing silicon nitride powder with about 20 vol% zirconium oxide and 4 vol% Al_2O_3 powders, then hot-pressing to achieve a fully dense plate. The plate is then given a subsequent anneal at 700°C for 5 hrs. in air. The zirconium oxynitride second-phase within several grain diameters of the surfaces is oxidized to monoclinic ZrO_2 with an accompanying increase in molar volume of about 4-5%. The expansion of the lattice in the surface regions gives rise to substantial compressive stresses on the surface (and significant tensile stresses in the interior). The oxidation increases the apparent surface toughness and flexural strength by about 25%.⁷ These results encouraged us to investigate the response of this material to particle impact.

3.2 Materials, Experiments, and Results

Lange provided two specimens each of oxidized and unoxidized Si_3N_4 -20 vol% ZrO_2 as halves of broken 4-point-bend specimens. Nominal dimensions were 3 x 6 x 18 mm. The surface finish of the unoxidized specimens was improved by polishing to make it comparable to the surface finish of the oxidized specimens.

Using 1.2-mm-diameter tungsten carbide spheres and a compressed air gun,⁸ we conducted a series of impact experiments at various velocities on oxidized (surface-strengthened) and unoxidized Si_3N_4 - ZrO_2 to determine the damage phenomenology, the threshold velocities for ring and radial cracks, and the rates of impact damage development.

At the lowest velocities, no damage could be detected at

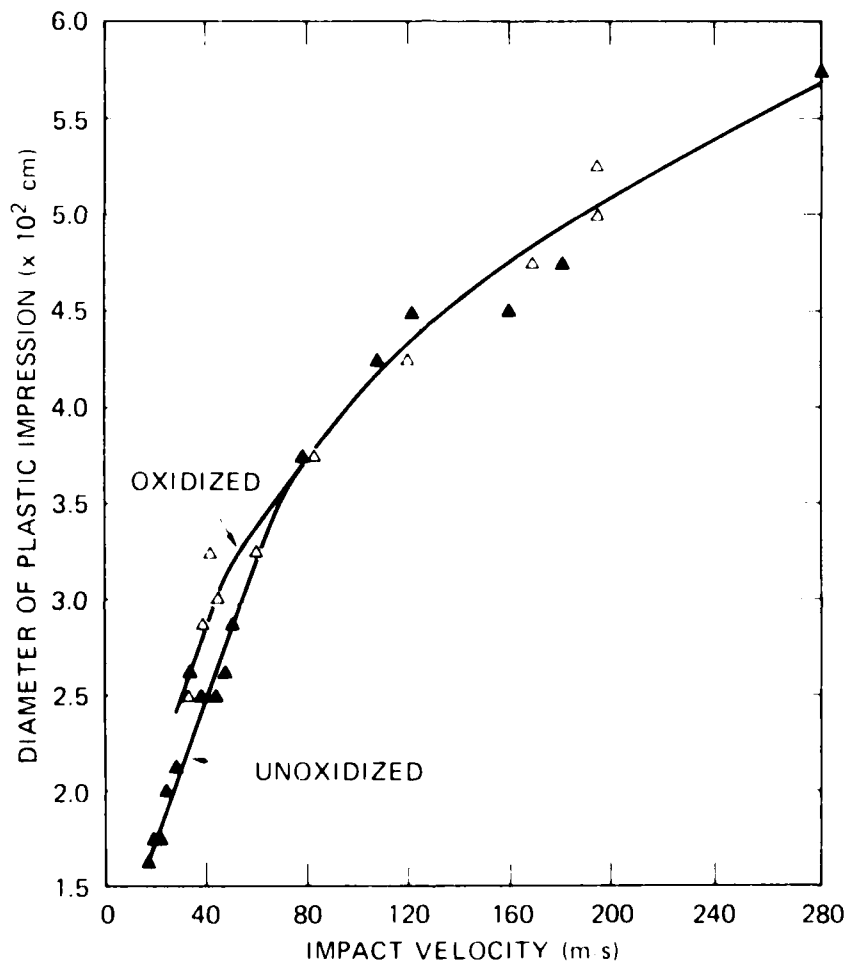
magnifications up to 400X. Slightly higher velocities produced a plastic impression, and at higher velocities, ring cracking began, followed by radial cracking at still higher velocities.

The size of the plastic impression increased monotonically with increasing impact velocity. A profilometer, used to measure the shapes of the impression, verified that plastic flow at the impact sites occurred at velocities well below those necessary for ring crack formation.* At low impact velocities, larger impressions were sustained by oxidized material, Figure 6, showing that the oxidation treatment decreased the dynamic hardness of the surface layers. At higher velocities (>80 m/s) impression diameters of oxidized and unoxidized material are nearly equivalent, indicating that the softening effect is confined to the surface layers.

A similar effect on quasi-static hardness was found in a series of diamond pyramid hardness indents at loads ranging from 0.1 to 20 kg. The average hardness of the oxidized material was 1200 kg/mm^2 , compared with a value of 1600 kg/mm^2 for unoxidized specimens. Again, a more pronounced softening in the surface layers of the oxidized specimens relative to the bulk was indicated by the hardness results (1000 kg/mm^2) at 0.1 and 0.2 kg indenter loads.

The threshold velocity for fracture damage in the oxidized material ($\sim 45 \text{ m/s}$) was substantially higher than for the unoxidized material ($\sim 17 \text{ m/s}$), and the amount of damage produced by a given higher velocity impact was significantly less. At an impact velocity of 45 m/s a portion of a single ring crack was produced in the oxidized

*This behavior is opposite that observed by A. G. Evans, University of California, Berkeley (private communication), and considerations of the stress distribution around a plastic contact show that radial cracks indeed should be expected because of large circumferential tensile stresses. Elastic contact produces large stresses in the radial direction and hence encourages ring cracking. In the elastic-plastic regime, however, the stress distribution may favor ring or radial cracks, and thereby account for the discrepancy in observed fracturing.



MA 4928 103

FIGURE 6 PLASTIC IMPRESSION DIAMETER VERSUS IMPACT VELOCITY FOR OXIDIZED AND UNOXIDIZED Si_3N_4 -20% ZrO_2

material, whereas several well-developed ring cracks were produced in the unoxidized specimens. Ring cracks became more numerous as velocity increased. Figure 7 shows the damage produced in the two materials by 145 m/s impact.* An annulus of cracked material developed about the center of the impact site. The annular area was always greater in the unoxidized material. At a velocity of 180 m/s, radial cracks appeared in the unoxidized material. No radial cracks were observed, however, in oxidized material at velocities up to 195 m/s. Figure 8 shows that the inner radius of the cracked zone is larger for the oxidized material, and the outer radius is smaller. Thus, for any given impact velocity, the damaged area in oxidized material is significantly smaller than in the untreated material.

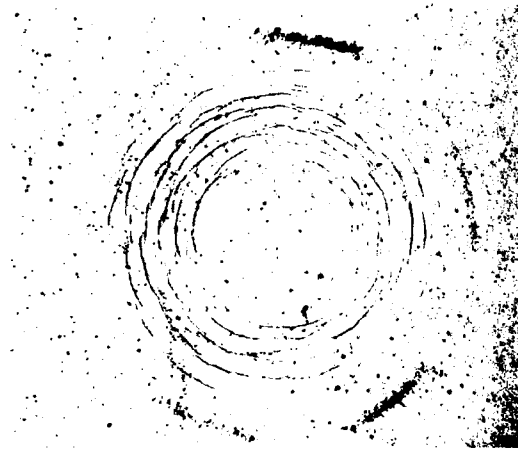
Several impact sites in oxidized and unoxidized material were sectioned, and the section surfaces were polished and examined with a microscope to determine the cracking patterns in the specimen interior. Both materials showed the Hertzian cone-shaped cracks.

3.3 Discussion

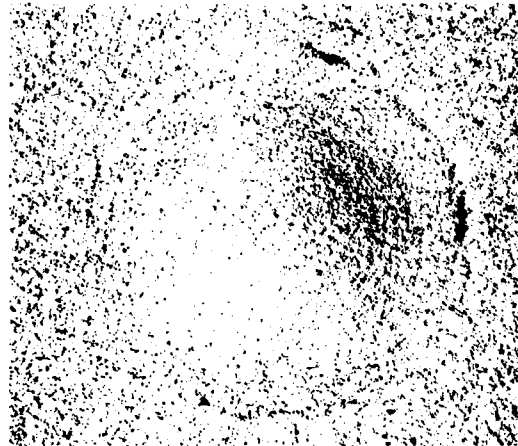
The observed enhancement of impact damage resistance could be attributable to oxidation-induced surface compressive stresses or to oxidation-induced softening or to both. However, the important aspect of the impact damage resistance is in the fracture propensity of the two materials. Ring cracks and radial cracks were initiated at lower levels and developed at more rapid rates in the unoxidized material, which suggests that the oxidation-induced surface compressive stresses inhibit and suppress fracture.

Although the experimental results indicate superiority of the oxidized material in resisting damage from an impacting particle, the use of oxidized material in high-temperature oxidizing environments,

*The halo that is evident in Figure 7 is shallow surface damage produced when the tungsten carbide sphere fragments and impacts the surface. Tungsten carbide spheres break at velocities of about 100 m/s and greater when impacted against these specimens.



UNOXIDIZED

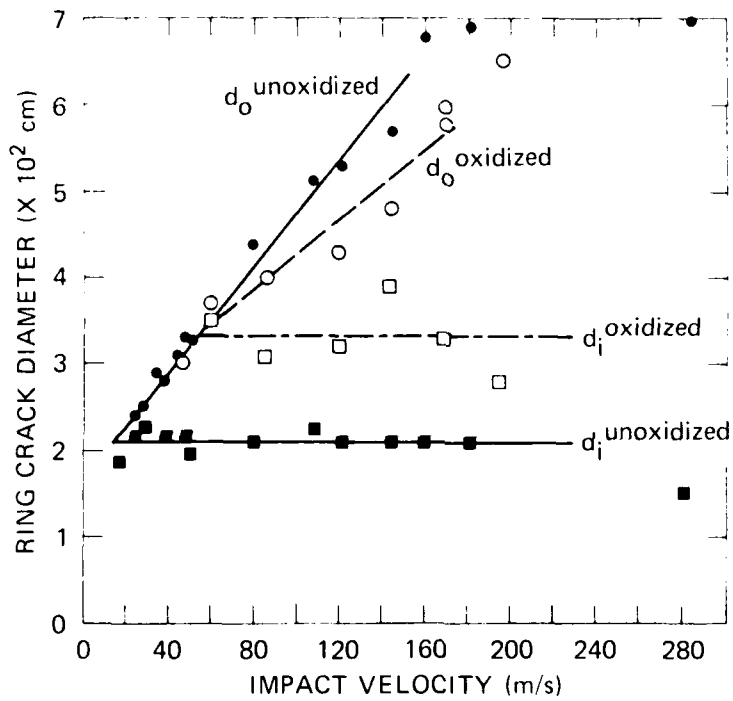


OXIDIZED

200 μm

500x

FIGURE 7. SURFACE DAMAGE PRODUCED BY PARTICLE IMPACT AT 145 m/s



MA-4928-100A

FIGURE 8 GROWTH OF DAMAGE ZONE WITH IMPACT VELOCITY FOR OXIDIZED AND UNOXIDIZED Si_3N_4 -20% vol % ZrO_2

such as those encountered by turbine blades, appears of doubtful benefit because previous impact tests indicate that over-oxidation increases erosion rates.¹

We note that the material used here was probably not optimal; other compositions and oxidation treatments could be expected to exhibit greater dynamic fracture resistance. Additional experiments on other oxidation-toughened materials and with particles of other sizes, shapes, types, angles of incidence, and velocities are suggested to confirm and further investigate these promising initial results.

4 PROGRESS IN DEVELOPING A PREDICTIVE CAPABILITY FOR HARD PARTICLE IMPACT DAMAGE IN CERAMICS

Development of a quantitative predictive capability for particle impact damage in ceramics requires a detailed knowledge of the stress field histories experienced by material in the vicinity of the impact site and mathematical expressions describing the development of plastic deformation and cracking. This section describes the procedures and results of a method we have developed for computing stress field histories and presents the rudiments of a computational fracture model.

4.1 Approach

Our approach in developing a predictive capability for particle impact damage in ceramics consists of the following tasks:

- (1) Establish an experiment that can be analyzed to allow identification and evaluation of the material properties governing resistance of semibrittle materials to fracture damage by particle impact. Experiments having the highest probability of success appeared to be those closely simulating particle impact conditions, but having a simple impact geometry to aid in interpretation and analysis. Thus, we performed experiments involving normal (90°) impact of a single, elastic sphere against a flat specimen surface.
- (2) Obtain an understanding of how fracture damage develops about an impact site. We studied damage phenomenology by performing experiments at various velocities so as to produce various levels of damage ranging from below incipient to surface fragmentation. By examining the impact sites and cross sections taken through the sites with a microscope we deduced how fracture damage evolves.
- (3) Describe quantitatively the deformation and fracture damage produced by particle impact. Definition of impact erosion properties requires a knowledge of the relationships between loading parameters and material failure response, and therefore a quantitative description of deformation

and fracture is required. We counted and measured the radial, ring, and lateral cracks at particle impact sites to obtain crack size distributions for various impact velocities.

- (4) Compute stress field histories produced in materials impacted by a solid particle. The stresses and strains and their variation with time and location in the target must be known in order to analyze the observed flow and fracture damage. Further, a procedure for computing stress field histories under particle impact is necessary as the basis for the predictive capability.
- (5) Construct a mathematical model of the fracture processes by making use of fracture mechanics concepts and correlations of fracture damage with computed stress histories. Write the model as a subroutine for the computational code used in the previous task to calculate the stress field history.
- (6) Verify the fracture model by using it in the stress field history code to simulate selected particle impact experiments. Compare computed and observed fracture damage, and modify the model until good agreement is obtained. Extract from the model the expressions and properties describing impact damage development.

Tasks 1 through 3 have been completed and the procedures and results are documented in References 1 and 8. Tungsten carbide spheres were accelerated in a pneumatic gun to velocities ranging from 10 to 250 m/s and made to perpendicularly impact polished surfaces of chemical-vapor-deposited zinc sulfide and hot pressed Si_3N_4 . The individual impacts produced various levels of damage in the form of plastic impressions and populations of several types of cracks. The fracture damage was quantified by counting and measuring individual cracks.

Damage threshold conditions and characteristic rates for crack nucleation and growth were deduced from the data. The shapes of the crack size distribution curves suggest that the size distribution of inherent flaws is exponential, consistent with the results of probability theory, and show that the growth law for radial cracks is similar in form to expressions derived from elastic energy balances.

The next step (Task 4) in developing the predictive capability is to compute the stress field histories experienced by ceramic plates impacted by a sphere, so that the quantitative fracture data can be correlated with the causative stress pulses (Task 5). During this reporting period the stress field history computation, Task 4, was completed and fracture model development, Task 5, was begun. This section presents the results of this work.

4.2 Calculation of the Stress Field History in a Plate Impacted by a Sphere

4.2.1 Background

Computation of the stress field history produced in a target material by an impacting particle is complicated and quite formidable, involving elastic and plastic deformation, dynamic effects, and the stress relaxation effects of cracks as they develop. Analytical solutions exist only for the most simple (and least interesting) of situations--namely, the static indentation elastic case in which no fracture occurs.^{9,10} Even in this case, however, there appears to be no simple single parameter that characterizes the stress field; that is, there is no parameter analogous to the stress intensity factor that characterizes the magnitude of the stress field at the tip of a crack.* Such a parameter would clearly be very useful in correlating stress field history with fracture damage and, hence, was sought during this present research year.

We considered therefore numerical methods and examined the various available advanced computer codes to determine (1) if the stress field history in a target impacted by a hard

*The nonlinearity arises because the contact area increases nonlinearly with pressure.

sphere had already been computed, and if not (2) whether such a computation appeared possible with an existing code. We found that the water drop impingement problem had been simulated by Rosenblatt, Ito,^{11,12} and others and that computations of impact by penetrators with noses of various shapes (including hemispherical) had also been completed.¹³ Rosenblatt and Eggum¹⁴ appear to have performed the only computation of hard sphere impact. These workers simulated the impact of a 400- μ m-dia. WC sphere onto a flat ZnS surface at 850 m/s. They assumed the sphere to be rigid, the ZnS to be elastic-perfectly plastic and to sustain no fracture, and the sphere-target interface to be frictionless. Under these assumptions they obtained the contact pressure and contact radius as a function of time, the growth of the plastic zone beneath the contact site, and the magnitude and directions of the tensile stresses outside the plastic zone. Although their results will be modified by the fracture activity that occurs in both the target and the sphere, the results are useful in interpreting, at least qualitatively, the observed fracture morphology in ZnS.¹⁵ We therefore proceeded on a similar path, using a 2-D Lagrangian wave propagation code to calculate the deformation and stress histories in our targets. Development of a reliable predictive capability, however, requires that the stress relaxation caused by the developing damage be accounted for. We are therefore also attempting to obtain a treatment for stress relaxation by appropriately modeling the fracture process, Section 4.3.

4.2.2 Computational Procedure

The particle impact experiments were simulated computationally using TROTT, a two-dimensional, Lagrangian, finite difference, wave propagation code written at SRI International.¹⁶ The calculational procedure is the standard leapfrog method of Von Neumann and Richtmyer,¹⁷ using artificial viscosity to

smooth shock fronts over several computational cells, which may be quadrilateral or triangular and treated as finite elements for mass and momentum calculations. The code can accommodate complicated material models because of its large storage capability per cell, but the code is simple and easily modified. Because of its simplicity, TROTT runs about three times faster than standard 2-D codes.

In preparation for the simulation, a slide line was inserted at the particle-target interface to allow the spherical impactor to start out not in contact with the target, then to penetrate an appropriate distance into the target with sliding occurring, and finally to separate from the target as the sphere rebounds. The surface of contact was modeled by a standard master/slave slide line (with both force and displacement condition) across the sphere-target interface. Before impact and after rebound, when the two surfaces are not in contact, the forces and displacements in the sphere and target are calculated independently. During contact, however, the force on both sides of the contact surface govern the motion of the master side of the slide line, and the displacement of the master side of the slide line governs the normal displacement of the slave side. Hence, the slave surface slides on the master surface.

The computational grids of the target and spheres were constructed to conform to a Cartesian coordinate system and to provide higher resolution in the area of contact where stress and strain gradients are steep. The target cells were nearly square and similar in size to neighboring cells. The largest cell dimension did not exceed the smallest dimension by more than 10%. Likewise, the areas of neighboring cells did not vary by more than 10%. The sphere was zoned by laying out a grid of horizontal and vertical lines that had the necessary resolution and cell size variation, rotating this network 90° and mapping

the network into a circle by means of the Joukowski transformation.¹⁸ This transformation $Z' = Z + b^2/Z$ in the complex plane maps circles into lines and is well known in the field of fluid mechanics. The resulting grids are shown in Figure 9.

We chose to simulate the impact of an 800- μ m-dia. tungsten carbide sphere with a plate of CVD ZnS at velocities of 5, 30, and 60 m/s. Cracking around the impact site and the concurrent stress relaxation were not treated in the initial simulations. These important effects will be taken into account in subsequent calculations by the dynamic fracture model being developed in Task 5 of this research program. The tungsten carbide sphere was treated as elastic, but plastic flow of the target was allowed to occur according to a stress-strain relation deduced from hardness tests. Using the method of Evans and Wilshaw,¹⁹ we characterized the quasistatic work hardening behavior of ZnS by plotting in log-log space the indentation pressure versus the normalized plastic impression diameter d/D , where d is the impression diameter and D is the diameter of the WC sphere, Figure 10. The slope was taken as an approximate value of the work hardening exponent, $n = 0.3$. The material properties used in the simulation are listed in Table I.

4.2.3 Results

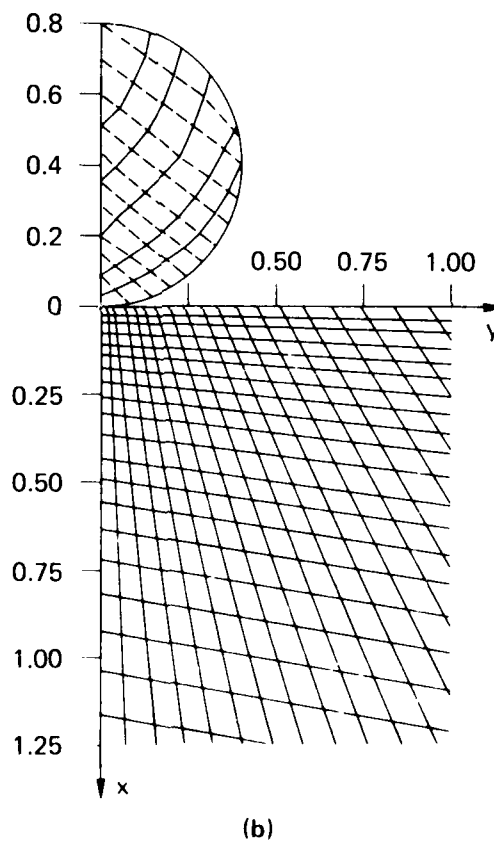
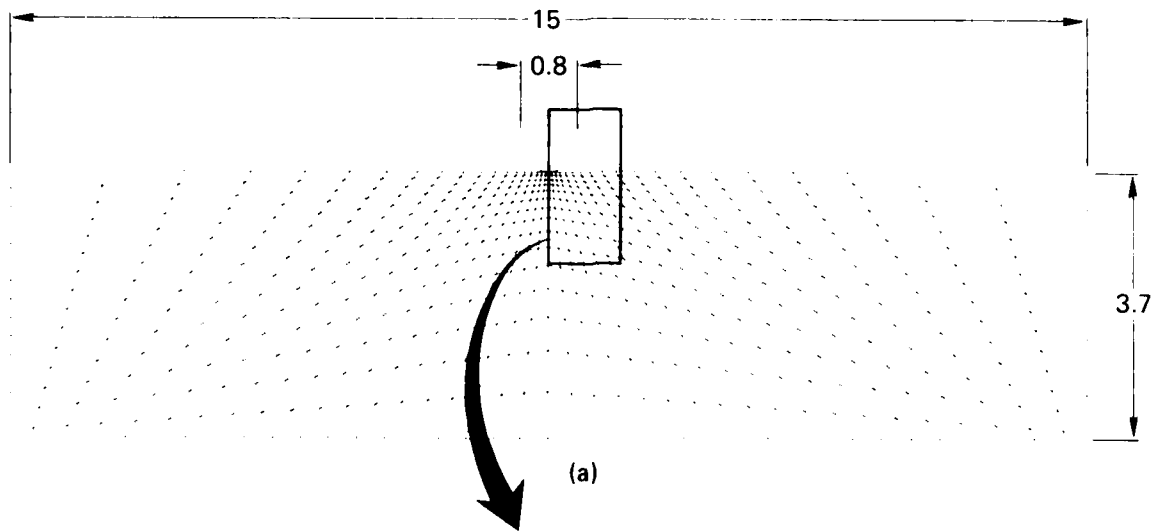
The computation simulated qualitatively all the important aspects of a particle impact event. The sphere approached the target at the prescribed velocity, made contact, and began to penetrate. The stresses in the target increased monotonically and when the yield strength was reached, material in the immediate vicinity of the impact site began to flow plastically. As the elastic sphere continued to penetrate, the elastically deformed zone expanded.

Sphere velocity decreased monotonically with increasing penetration, reached zero, then became negative (i.e., rebounded),

Table I

MATERIAL PROPERTIES USED IN PARTICLE IMPACT SIMULATION

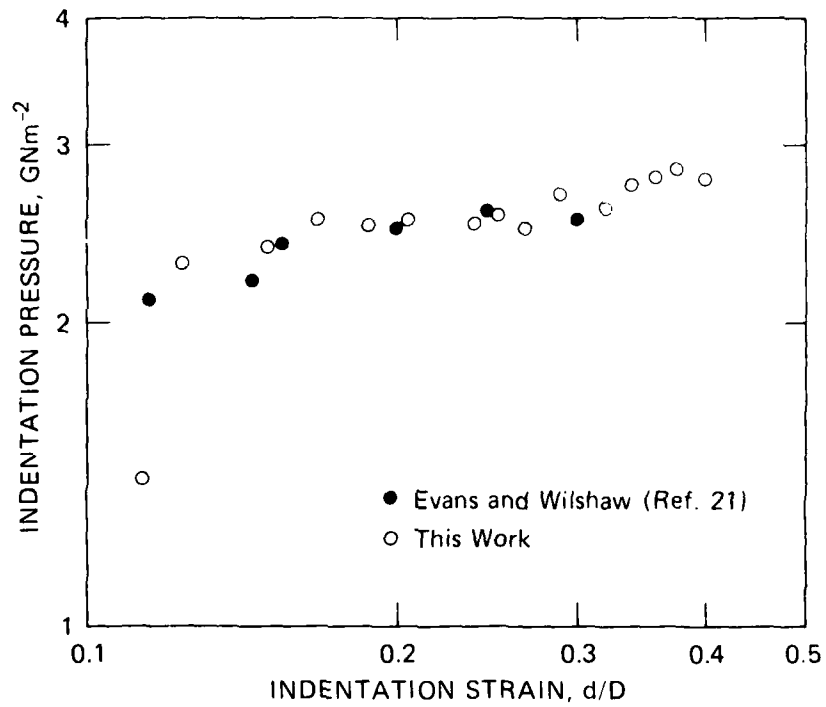
	Eulk Modulus K(dynes cm ⁻²)	Shear Modulus μ(dynes cm ⁻²)	Work Hardening Exponent	Density ρ(g cm ⁻³)	Yield Strength σ _y (dynes cm ⁻²)	Grüneisen's Ratio
ZnS	7.19 x 10 ¹²	3.18 x 10 ¹²	0.3	4.08	3 x 10 ¹⁰	-
WC	4.49 x 10 ¹²	2.82 x 10 ¹²	-	15.0	1 x 10 ⁹⁹	2



For clarity, the grid shown in (a) is twice as coarse as actual grid (shown in (b)).
All dimensions in millimeters.

MA 4928-108

FIGURE 9 COMPUTATIONAL GRIDS USED IN SIMULATING A SPHERE IMPACTING A PLATE



MA-4928-110

FIGURE 10 STRESS-STRAIN CURVE FOR ZnS INDENTED WITH AN 800- μm -dia. WC SPHERE

accelerating in the direction opposite the impact direction and finally reaching a steady-state rebound velocity as it lost contact with the target. Crater depth and diameter relaxed somewhat from the maximum values attained at deepest sphere penetration, and a residual stress field remained about the impact site.

To verify the quantitative fidelity of the computation, we compared, wherever possible, computed results with measurements we made in the experiments. Table II compares computed and observed sphere rebound velocities, crater diameters, and crater depths at three conditions of impact velocity.

The computational results agree very well with the measurements from experiment for the low velocity impact case, but agreement worsens with increasing impact velocity. This is to be expected because the extent of fracture damage increases with velocity, and fracture was not accounted for in these calculations. Observed crater diameters were smaller than computed, possibly because the occurrence of radial cracks tends to relax the tangential stresses and hence reduce the extent of plastic flow. The measured crater depths, on the other hand, were greater than computed, suggesting that the occurrence of radial cracks facilitates sphere penetration. The comparisons in Table II lend credence to the calculated stress field histories, selected samples of which are displayed in Figures 11 and 12.

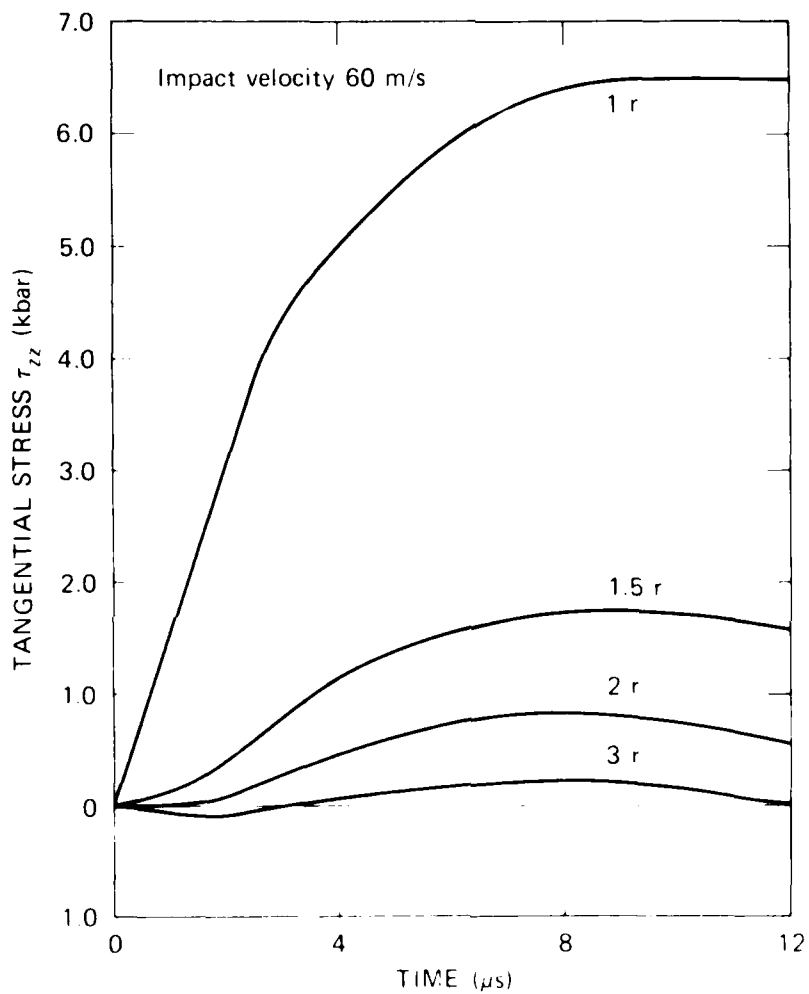
The variation in tangential stress with time at several distances from the impact crater is shown in Figure 11 for a 60 m/s impact. The tangential stress rises slowly and reaches a maximum at about 8 μ s after impact, and then decreases even more slowly. The value of the maximum falls off strongly with distance. At large distances (three crater radii) from the impact axis, the tangential stress is initially weakly compressive.

Figure 12 indicates the variation of peak tangential tensile stress with distance from the impact site center for three

Table 11

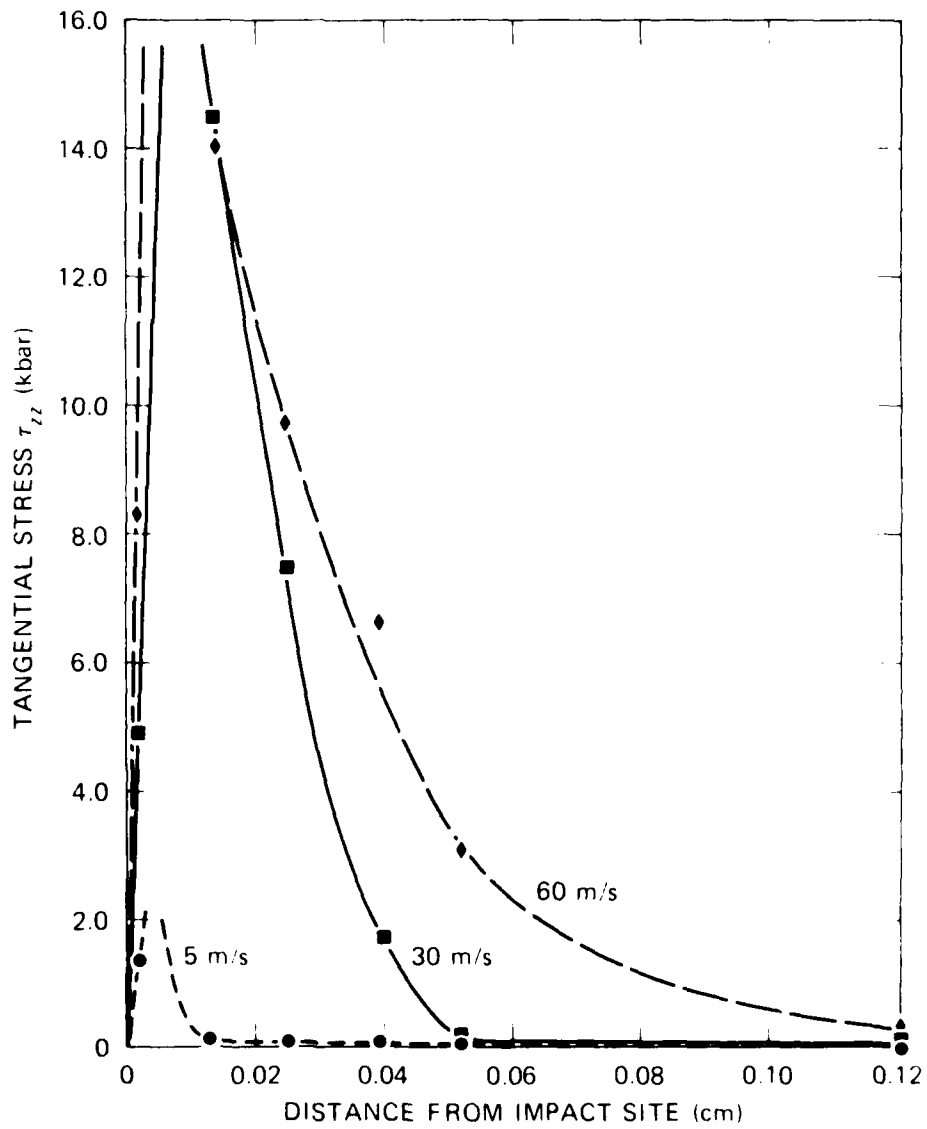
COMPARISON OF COMPUTED AND OBSERVED RESULTS
OF PARTICLE IMPACT EXPERIMENTS

	IMPACT VELOCITY		
	5 m/s	30 m/s	60 m/s
Rebound velocity (m/s)			
Observed	4.8	16.2	30
Computed	4.9	13.1	20.7
Crater diameter (mm)			
Observed	None observed	0.24 ± 0.01	0.36 ± 0.01
Computed	0	0.25	0.47
Crater depth (mm)			
Observed	None observed	0.014 ± 0.001	0.034 ± 0.001
Computed	0	0.012	0.026



MA 4926 112

FIGURE 11 VARIATION OF TANGENTIAL TENSILE STRESS WITH TIME AT 1, 1.5, 2, AND 3 CRATER RADII (r) FROM IMPACT SITE



MA-4928-113

FIGURE 12 VARIATION OF PEAK TANGENTIAL TENSILE STRESS WITH DISTANCE FROM IMPACT SITE FOR THREE IMPACT VELOCITIES

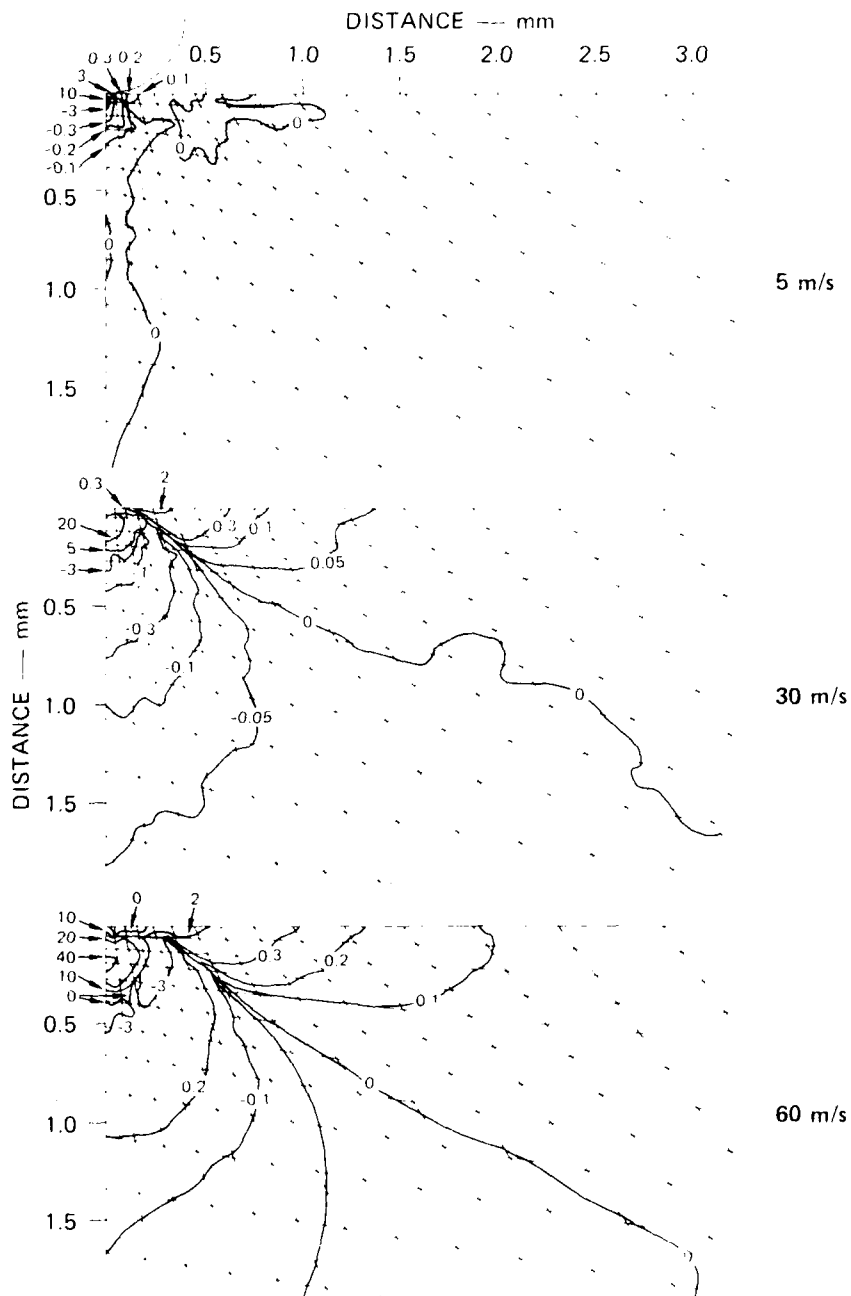
velocities. Stress rises more sharply with distance for higher impact velocities and falls off more gradually. Also, the peak stress values increase with impact velocity, even though the resolution of the computer printout was not fine enough to capture the maxima of the stress-distance curves in Figure 12. Finally, the maxima appear to occur further from the impact site center for higher velocity impacts.

The computed residual stress fields produced by impact at the three velocities are shown in Figure 13. Compressive residual stresses are predicted near the specimen surface and extend several sphere radii from the impact site. A residual tensile stress field is produced beneath the impact site. The spatial extent of both fields increases with impact velocity. Maximum values of residual tensile stresses for the 60 m/s impact are about 40 kbar and occur approximately one half sphere radius beneath the impact site. Compressive residual stresses reach maxima of about 2 kbar for the 30 m/s and 60 m/s impact and occur close to the target surface at about one sphere radius from the impact site center.

We conclude from the agreement between computed and observed crater dimensions that the stress field histories produced by hard particle impact are computed reliably and in sufficient detail so that the TROTT code is a suitable basis for the predictive damage capability. In Section 4.3 we construct a computational model for radial cracking around impact sites and write it in a form suitable for incorporation into the TROTT code.

4.3 Construction of a Computational Fracture Model

For making quantitative predictions of the extent of fracture produced in a target impacted by a particle, mathematical expressions are required that relate fracture damage to the causative



MA 4928 109

FIGURE 13 RESIDUAL STRESS FIELDS IN ZnS AFTER IMPACT WITH A 0.8-mm-dia TUNGSTEN CARBIDE SPHERE AT THREE VELOCITIES

Values are pressure = $\frac{\sigma_1 + \sigma_2 + \sigma_3}{3}$ in kbar, negative values are tensile

stress and strain field histories. The mathematical expressions we have developed describe the various stages of the fracture process and, taken together, constitute the fracture model.

To be reliable, the fracture model must be based on the actual impact-induced physical events occurring in the target that lead to the final fracture damage. The phenomenology of fracture in ZnS under single particle impact was deduced from observations of the damage produced by impact at various velocities, and is described in the following subsection. Subsection 4.3.2 develops the expressions that describe various aspects of the phenomenology and discusses the parameters in these expressions and their role as dynamic fracture properties. Section 4.4 discusses incorporation of the model into the wave propagation code described in Section 4.2, and recommends research tasks for future programs.

4.3.1 Phenomenology of Particle Damage in ZnS

The sequence of cracking events in ZnS was determined by direct optical observation and by acoustic emission under quasi-static indentation with a WC sphere¹⁹ and also was inferred from posttest examination of impacted specimens.⁸ The sequence is as follows: As the sphere is pushed into the ZnS surface, plastic flow occurs under the contact area and a permanent impression forms. The diameter increases with increasing load, and is linear in a log-log plot, Figure 10. At a certain threshold load, about five roughly equispaced, shallow surface cracks form and spread radially outward from the crater periphery on planes perpendicular to the surface. At increasing loads these cracks increase in length and slightly in depth, maintaining a thumb-nail-shaped profile and additional radial cracks appear. The number of large (~200 μ m) radial cracks attains a maximum of 10 to 12, whereas smaller radials increase in number beyond 50 and maintain an exponential size distribution.

At loads higher than those required to form radial cracks,

one or two penny-shaped cracks containing the indentation axis form beneath the plastically impressed surface. These cracks, called median vents, expand radially outward and often join with the radial cracks.

Still higher loads are required to produce lateral vents--cracks that form and propagate parallel to the indented surface between the radial cracks. The number and sizes of lateral cracks increase with load, reaching maximum values similar to those of the radial cracks.

As the load is removed, all three types of cracks grow further. The depth, and to a lesser extent the diameter, of the plastic impression recovers somewhat, but residual plastic strains apparently hold the radial cracks open. Sectioning studies show a heavily deformed or finely fractured zone immediately below the impression, and often two or three levels of lateral cracks.

4.3.2 Rudiments of the Fracture Model

The observations described in the previous section suggest that the fracture damage produced in ZnS by particle impact occurs by the nucleation and growth of cracks in planes and directions dictated by the stress field histories in the vicinity of the impact site. Thus, the computational fracture model should consist of an expression describing crack nucleation for computing the number of cracks produced by a given impact, and an expression describing crack growth for computing the size of the nucleated cracks. In addition it is necessary to treat the relaxation of the impact-induced stress field that results when cracks develop.

Crack nucleation is the result of activation of pre-existing flaws during passage of the stress pulse. Flaws (or weak sites) such as intergranular or transgranular cracks, pores, grain boundaries or triple points, and machining and grinding

damage are inherent in materials, and these flaws may become unstable and propagate when traversed by a stress pulse of sufficient amplitude and duration. Linear elastic fracture mechanics relates the critical stress amplitude to the crack length by the stress intensity, and shows that the larger the preexisting crack, the lower the continuum stress required to activate it. For the situation where the load is not quasistatic, but rather is applied as a short-lived stress pulse, the duration of the stress pulse must be considered in crack instability analyses.²⁰

Considerations of stress intensity histories experienced by cracks whose lengths are comparable to the distance a stress wave can propagate during the pulse life suggest that the attainment of a critical level of stress is necessary, but not sufficient, for crack instability. A sufficient condition is that the stress level be attained for some minimum time. Experimental results on several polymers and structural metallic alloys support this premise.²¹

Thus the expression for crack nucleation must relate the number N and sizes R of inherent flaws, the resistance of the material to crack activation (taken as a fracture toughness appropriate for particle impact loading rates, $K_{I\dot{d}}$), and the minimum time for instability t_{min} to the amplitude σ , duration T_0 , and perhaps the shape δ of the stress pulse. We can write the general form

$$dN/dt = f(N, R, K_{I\dot{d}}, t_{min}, \sigma, T_0, \delta) \quad (4-1)$$

for the nucleation function.

In our previous work on ZnS¹⁹ we showed that the shape of the flaw size distribution is exponential, having the form

$$N_g = N_0 \exp(-R/R_n) \quad (4-2)$$

where N_g is the cumulative number of flaws per unit volume with radii greater than R , N_0 is the total number of flaws, and R_n

is a size parameter. The quasistatic fracture toughness, K_{Ic} , has been determined in previous experiments^{22,23} to be $0.75 \pm 0.01 \text{ MN m}^{-3/2}$, and little rate effect is expected in this semibrittle material.

The approximate functional form of Eq. (4-1) will be established in future work by correlating the measured crack size distributions from the experiments in Reference 8 with the computed stress field histories described in Section 4.2.

Several expressions for crack growth have been postulated from theoretical considerations.²⁴⁻²⁶ The crack size distributions predicted by these expressions are illustrated in Reference 8 and compared with measured crack size distributions at impact sites in ZnS. Since all theoretical expressions result in distributions similar to that observed, we chose the simplest expression for the present fracture model, namely,

$$dR/dt = kC_{\ell} \quad (4.3)$$

where dR/dt is the crack growth rate, C_{ℓ} is the longitudinal wave speed, and k is a constant between zero and 1. In previous work on dynamic brittle rock fracture,²⁷ the theoretical value²⁴ $k = 0.38$ produced good agreement between computed and observed damage.

As fracture damage develops, the stresses in the target relax. When radial cracks form and grow, the tensile stresses on their surfaces fall to zero and this unloading information is communicated to the surrounding material by a wave that propagates away from the newly formed crack. Tensile stresses in the plane of the crack, however, may remain high, so that the stress relaxation process may be highly anisotropic. Thus the occurrence of cracking modifies importantly the stress field history produced by an impacting sphere, and may explain the increasing divergence with impact velocity (increasing cracking) of computed and observed crater dimensions and rebound velocities (Table II). Clearly, a reliable predictive capability requires

that the effect of developing fracture damage on the state of stress be continuously accounted for during a computational simulation.

The basis for the treatment of crack-induced stress relaxation is the concept of a two-component system: solid material, and void inside the open cracks. The specific volume of the system changes when loaded; this change is due partially to strain in the solid and partially to change in the void volume. The void volume calculation follows the analysis of Sneddon²⁸ for a penny-shaped crack in an elastic material. During the wave propagation calculation, the following sequence of events is envisaged while the material is in tension:

- (a) Initial tensile loads cause only elastic volume changes in the solid until a threshold stress (equal to the dynamic fracture strength) is reached.
- (b) When the stress exceeds the fracture threshold, cracks begin to nucleate and grow, and the void volume produced by the cracks acts to decrease the volume change required of the solid. Thus the tensile stress in the solid is lower than it would be for undamaged material under the same volume change; hence, the effective modulus of the solid has decreased.
- (c) With increasing stress and continuing volume change, a point is reached where the void volume increase just equals the applied volume change. Here there is no change in solid volume and hence no change in tensile stress: The stress-volume path has reached a peak and the effective modulus is zero.
- (d) With further volume changes, the increase of void volume (by growth and nucleation of cracks) tends to exceed the applied volume change. Then the solid volume change is negative and the tensile stress is decreasing. The effective modulus is negative during this period.

- (e) If compressive volume changes occur at any time, there will usually be a decrease in both void volume and solid volume. Then the effective modulus is positive as in (a).
- (f) If no net volume change occurs, there will usually be an increase in void volume and a corresponding decrease in solid volume: The effective modulus in such a case is infinite.

The preceding sequence of events is treated in the present formulation of the behavior of material undergoing fracture. A derivation of the effect of damage on the material stiffness is given below to indicate the basis of the method. Here the case is considered in which flaws are present but no nucleation or growth of cracks occurs: The resulting modulus is that which is appropriate for a residual strength calculation. The fundamental relation is that the total volume change is the sum of solid and void volume changes:

$$\Delta V = \Delta V_S + \Delta V_V. \quad (4-4)$$

The void volume change is derived from the analysis of Sneddon²⁸ for the opening of a penny-shaped crack in an elastic medium under uniform tension. The half-opening of the crack faces is

$$\delta = \frac{4(1 - \nu^2)c\sigma}{\pi E}$$

where c is the half crack length

σ is the stress applied normal to the crack plane

E is Young's modulus

ν is Poisson's ratio.

The void within the crack faces is an ellipsoid with semiaxes c , c and δ , so the volume is

$$V_{ic} = \frac{4}{3}\pi\delta c^2 = \frac{16(1 - \nu^2)c^3\sigma}{3\pi E} \quad (4-5)$$

To determine the total relative crack volume, a sum is made over all cracks

$$V_V = \sum_i N_i V_{ic}$$

where N_i is the number of cracks of volume V_{ic} per unit volume. Then Eq. (4-4) becomes

$$\frac{\Delta V}{V} = \frac{\Delta \sigma}{(K + \frac{4}{3}\mu)V} + \frac{16(1 - \nu^2)\Delta \sigma}{3E} \sum_i N_i c_i^3 \quad (4-6)$$

where $\Delta \sigma$ is a change in stress

K, μ are bulk and shear moduli

V is the total specific volume.

Dividing Eq. (4-6) by $\Delta \sigma$, we derive an effective modulus M .

$$\frac{1}{M} = \frac{V_s/V}{K + \frac{4}{3}\mu} + \frac{16(1 - \nu^2)}{3E} \sum_i N_i c_i^3. \quad (4-7)$$

This compliance is similar to that which would be obtained for a composite made of solid material plus void. The term $K + (4/3)\mu$ is the stiffness of the solid and V_s/V is its volume fraction. The last term on the right in Eq. (4-7) must be interpreted then as the compliance of the cracks. This expression shows that the compliance of the composite increases with increasing void fraction, that is, increasing number and/or increasing size of cracks. Since both the strain in the solid and the void volume are tensor quantities, the stress relaxation is appropriately anisotropic.

4.4 Future Work

The final steps in the development of the predictive capability for particle-impact-induced fracture damage are to evaluate the nucleation function, Eq. (4.1); insert the fracture model (Section 4.3) into the TROTT code (Section 4.2); simulate computationally several selected particle impact experiments; compare the computed and observed fracture damage; and, if necessary, modify the expressions and parameters in the model to attain good agreement.

The nucleation function, Eq. (4.1), should be evaluated by correlating computed stress-strain field histories for experiments of several impact velocities with measured radial crack size

distributions. We expect these correlations to be difficult because of the high gradients in stress and strain near the impact site. More suitable experiments are flat plate impact experiments such as those reported in Reference 29, because the specimens contain relatively large volumes of material that experience nearly constant stress and strain histories. Thus, statistical data on the number and sizes of cracks can be obtained for correlation with a stress or strain state. Limited data on ZnS exist ²⁹ and should be examined to help in the correlations.

The fracture model presented in Section 4.3 contains only one orientation of cracks and treats only an exponential crack size distribution. The model should be extended to pertain to cracks in three orthogonal directions so that radial, ring, and lateral cracks can be treated simultaneously. Furthermore, since nonexponential crack size distributions have been observed after considerable crack growth, appropriate mathematical descriptions of the distributions should be developed and incorporated into the model.

These modifications have been studied extensively to determine their feasibility and possible implementation procedures. The use of three orientations of cracks introduces significant convergence problems in the stress and damage calculational algorithm. Currently, with one crack orientation, an iteration procedure is used to determine one unknown strain from the nucleation, growth, and crack-opening functions. With three orientations, an iteration procedure for three unknowns will be required. Because of the nonlinearity of the functions, convergence of the iterations will be difficult to obtain, but techniques developed at SRI International for similar problems may be applicable.

Representation of more complex crack size distributions can be done in several ways. One method we have used in other cases is to describe the distribution by a series of N-R values instead of by an analytic function. This method is straightforward to use, but it adds greatly to the computer storage required. An alternative method

is to use a higher order function to represent the crack size distribution; this method requires derivation of nucleation and growth laws for each of the parameters of the distribution. A third alternative is a combination of the above: Describe the crack size distribution by a series of exponential functions, each governing a narrow range of crack radii. These three possibilities should be explored for their appropriateness to the problem and the efficiency with which they can be executed.

These modifications should be done concurrently with work to correlate the nucleation and growth expressions with observed damage.

4.4 Summary

Considerable progress has been made in developing a predictive capability for fracture damage in ceramics produced by particle impact.

A two-dimensional Lagrangian, finite difference, wave propagation code, TROTT, was provided with a slide line capability and used to simulate the impact of an 800- μm -dia. WC sphere and a ZnS plate at velocities of 5, 30, and 60 m/s. Plastic flow was allowed to occur according to an experimentally determined stress-strain relation, but cracking and the associated stress relaxation were not treated in these initial calculations. The computation simulated qualitatively all of the important aspects of a particle impact event, and gave good quantitative agreement with experimental measurements of rebound velocity and crater dimensions.

Mathematical expressions that describe crack development in ZnS under particle impact load histories were deduced from observations of the number and sizes of radial cracks produced by impact at various velocities. These expressions treat damage development as a crack nucleation and growth phenomenon and constitute a computational fracture model that, written as a subroutine, can be used in conjunction with the wave propagation code to calculate the extent of fracture damage resulting from a given particle impact. The parameters in the model, because they are material-specific and hence act as dynamic fracture properties, can be used to rank and evaluate candidate materials for various impact erosion applications.

Objectives of future work are to establish the functional form of the crack nucleation expression, to incorporate the fracture model in the wave propagation code, and to simulate computationally selected particle impact experiments.

REFERENCES

1. K. C. Dao, D. A. Shockey, L. Seaman, D. R. Curran, and D. C. Rowlette, "Particle Impact Damage to Steel on Nitride," Annual Report, Part III, to Office of Naval Research, Arlington, VA, on Contract N00014-76-C-0667, May 1979 (to be published in the J. Amer. Ceram. Soc.).
2. J. M. Winner, I. Bransky, and N. M. Lellan, "Impact Resistance of Structural Ceramics, Part II Ballistics Test," Annual Report, Air Force Materials Laboratory, AFML-OR-79-1, AFM-79-06-001, December 1976.
3. B. R. Lawn and T. R. Wilshaw, *J. Mater. Sci.*, **10**, 1039 (1975).
4. A. G. Evans and T. R. Wilshaw, *Acta Met.*, **23**, 939 (1975).
5. P. Labor, *The Hardness of Metals* (Clarendon, Oxford, 1970).
6. C. J. Studman and J. L. Field, *J. Phys. In Appl. Phys.*, **9**, 8 (1976).
7. F. F. Lange, "Compressive Surface Stresses Developed in Ceramics by an Oxidation-Induced Phase Change," Technical Report No. 78, submitted to Office of Naval Research, on Contract N00014-76-C-0667, Rockwell International Science Center, Thousand Oaks, California (July 1978); *J. Amer. Ceram. Soc.*, in press.
8. D. A. Shockey, K. C. Dao, L. Seaman, and D. R. Curran, "Nucleation and Growth of Cracks in CVD ZnS Under Particle Impact," Annual Report, Part II, to Office of Naval Research, Contract N00014-76-C-0657 (April 1979).
9. H. Hertz, *Hertz's Miscellaneous Papers* (MacMillan, London, 1896); also M. T. Huber, *Am. Physik*, **14**, 153 (1904).
10. B. Lawn and T. R. Wilshaw, *J. Mater. Sci.*, **10**, 1039 (1975).
11. M. Rosenblatt, Y. M. Ito and L. De Angelo, "Numerical Simulation of Ceramic Target Response to Water Drop Impacts including Effects of Surface Flaws and Pores," *Proc. 5th Int. Conf. on Erosion by Solid and Liquid Impact*, p. 4-1, August 1979.
12. M. Rosenblatt, Y. M. Ito, and G. E. Eggum, "Analysis of Brittle Target Fracture from a Subsonic Water Drop Impact," in *Erosion: Prevention and Useful Applications*, ASTM STP 664, W. F. Aylor, Ed. (American Society for Testing and Materials, 1979), pp. 2-18, 20.
13. M. L. Wilkins, "Mechanics of Penetration and Perforation," *Int. J. Engng Sci.*, **16**, 378-807 (1978).
14. M. Rosenblatt and G. R. Eggum, Unpublished work at California Research and Technology, Inc., Woodland Hills, CA (1976).

END

DATE
FILMED

5-8-1

DTIC